Research Article Vol. 13, No. 7 / 1 Jul 2022 / Biomedical Optics Express 3904
Biomedical Optics EXPRESS

Automated wide-field malaria parasite infection detection using Fourier ptychography on stain-free thin-smears

OSMAN AKCAKIR,[1,*] LUTFI KADIR CELEBI,[1,2] MOHD KAMIL,[1] AND AHMED S. I. ALY[1]

[1]*Beykoz Institute of Life Sciences and Biotechnology (BILSAB), Bezmialem Vakif University, 34820 Istanbul, Turkey*
[2]*Istanbul Technical University (ITU), Electronics and Communication Engineering Department, Biomedical Engineering Program, 34467 Istanbul, Turkey*
[*]*oakcakir@bezmialem.edu.tr*

Abstract: Diagnosis of malaria in endemic areas is hampered by the lack of a rapid, stain-free and sensitive method to directly identify parasites in peripheral blood. Herein, we report the use of Fourier ptychography to generate wide-field high-resolution quantitative phase images of erythrocytes infected with malaria parasites, from a whole blood sample. We are able to image thousands of erythrocytes (red blood cells) in a single field of view and make a determination of infection status of the quantitative phase image of each segmented cell based on machine learning (random forest) and deep learning (VGG16) models. Our random forest model makes use of morphology and texture based features of the quantitative phase images. In order to label the quantitative images of the cells as either infected or uninfected before training the models, we make use of a *Plasmodium berghei* strain expressing GFP (green fluorescent protein) in all life cycle stages. By overlaying the fluorescence image with the quantitative phase image we could identify the infected subpopulation of erythrocytes for labelling purposes. Our machine learning model (random forest) achieved 91% specificity and 72% sensitivity while our deep learning model (VGG16) achieved 98% specificity and 57% sensitivity. These results highlight the potential for quantitative phase imaging coupled with artificial intelligence to develop an easy to use platform for the rapid and sensitive diagnosis of malaria.

1. Introduction

Malaria is a disease caused by the *Plasmodium* genus of parasite. This mosquito-borne parasite infects the blood of its host causing painful symptoms and sometimes death. During a blood meal, the infected mosquito transmits the parasite as sporozoites from its salivary glands into the human host thereby initiating infection [1]. Malaria is endemic to many parts of the world, and claimed 409000 people in the year 2019, with 386000 of these deaths occurring in Africa [2]. Young children are particularly effected by this disease with 266100 of the deaths occurring in the population that is under 5 years of age in 2018 [3]. Improved diagnostic methods amenable to use in resource poor areas could save the lives of many so there is intense interest in developing new technologies for this purpose.

Malaria diagnostics are mainly of three types:1. antigen based Rapid Diagnostic Tests (RTD) [4], 2. DNA based PCR (Polymerase Chain Reaction) tests [5], 3. Microscopy based imaging tests [4,5]. RTD results can be read without any instruments but are limited in that the measurement is qualitative. Each disposable test kit is also relatively expensive. PCR testing is very sensitive but requires expensive reagents and is time consuming. Standard microscopy approaches requiring a high magnification objective and skilled microscopist are still the gold standard. These methods call for Giemsa staining of blood smear samples with subsequent manual counting of infected

#448099 https://doi.org/10.1364/BOE.448099
Journal © 2022 Received 11 Nov 2021; revised 28 Jan 2022; accepted 28 Jan 2022; published 15 Jun 2022

Biomedical Optics EXPRESS

cells. Being able to forego the staining would reduce the cost and sample preparation time, increasing the practicality of testing. Having an automated method in addition would preclude the necessity of having trained microscopists, which are in limited supply, and would thereby increase the availability of testing.

Stain-free methods however require different measurement modalities in order to generate contrast in the sample measurement and distinguish infected from non-infected cells. Erythrocyte infection by the parasite proceeds in stages starting with the ring stage and continuing to the trophozoite and schizont stages [1]. A recent spectroscopic method combining UV-Vis (ultraviolet-visible) and NIR (near infra-red) wavelength regions shows promise in detecting low-level ring-stage parasitemia [6]. Surface-enhanced raman spectroscopy (SERS) has been applied to plasmodium infected erythrocytes (red blood cells) showed a spectral difference between the ring stage and the trophozoite/schizoid stages [7]. A magnetic technique referred to as rotating-crystal magneto-optical diagnostics (RMOD) has measured the hemozoin content of infected cells and was shown to be a sensitive detector of parasitemia level in infected organisms [8]. An imaging method based on a UV microscopy method including deep-UV imaging has demonstrated parasitemia detection and quantification including ring-stage detection [9], though this required specialized optics. In-line holographic imaging was also used to detect infected cells and train machine learning algorithms to automatically classify cells [10]. For the identification of infection by motile parasites, a motility-based method using holographic speckle analysis has been developed by Zhang *et al.* [11].

Quantitative phase imaging is another stain-free optical method that has been investigated recently. Quantitative phase imaging has been shown to be an effective imaging modality in a variety of cell and tissue types and for a range of diseases [12,13]. The measured quantitative phase image reflects a combination of the refractive index and thickness of the sample pixel by pixel. Together these features determine the 2D mass distribution profile over each of the sample cells. Morphological and structural changes of erythrocytes due to infection of the malarial parasite have been shown to be reflected in changes in the quantitative phase image of these cells [14,15]. In Moon *et al.* [16] digital shearing interferometry was used to generate the gradient phase and amplitude information from which 6 features were chosen to identify healthy cells and cells infected with malarial parasite. Anand *et al.* [17] measured the correlation coefficient of the cross-sectional thickness profiles of erythrocytes collected on a digital holographic interferometric microscope and then numerically reconstructed them at varying axial distances. They found that plasmodium infected erythrocytes had a lower correlation coefficient and that this metric could be used to differentiate infected from non-infected erythrocytes. In another work Anand *et al.* [18] used Gabor wavelet filtering of quantitative phase images of erythrocytes before applying morphology based feature extraction to distinguish between cells with stomatocyte, discocyte and echinocyte morphologies. Park *et al.* measured *Plasmodium falciparum* infected cells originating from culture for the trophozoite and schizont infection stages using a quantitative phase spectroscopy microscope to measure quantitative phase images [19]. They used morphological features extracted from the quantitative phase images to train a machine learning model to distinguish infected from non-infected erythrocytes as well as distinguish between the infectious stages (except for the ring stage). Ugele *et al.* developed a flow cell to flow sphered erythrocytes including infected erythrocytes through the detection area of a digital holographic microscope [20]. The quantitative phase images were examined by analyzing the optical height variance of each erythrocyte. In addition to the mentioned studies on the spatial distributions of the phase profiles of healthy and diseased cells, spatio-temporal membrane fluctuations in healthy and diseased cells have also been studied using quantitative phase imaging [21–23].

Our study differs from previous work using quantitative phase imaging for malaria parasite infection detection in three important ways: 1. we are measuring samples from whole blood withdrawn from an infected organism (rat) containing *all* infectious stages, 2. we are using

Biomedical Optics EXPRESS

the quick and simple thin-smear technique already practiced in the field for preparing the slide samples (i.e. our samples were dried on a slide and not maintained in solution), 3. we use the Fourier ptychography technique with a low-magnification objective lens allowing thousands of erythrocytes to be imaged at high-resolution in one field of view, and then automatically classify each segmented cell as either infected or uninfected. While there are other methods that make standard quantitative phase imaging methods (*e.g.* digital holography) high-throughput, like flow cytometry and scanning based methods, these involve moving parts, have increased mechanical complexity and may be less amenable to deployment and servicing in resource-poor settings.

Fourier ptychography is a computational imaging technique that uses a set of images collected with a variety of illumination angles to reconstruct a quantitative phase image at high-resolution [24]. Invented in 2013, this technique has seen growing research interest in methodologies and applications [25,26]. The quantitative phase is computed using numerical phase retrieval techniques based on the phase diversity of the set of images. The phase is not directly measured in Fourier ptychography but rather iteratively computed using an alternating projection algorithm in the original implementation. The high-resolution complex solution is constrained in the real space by the low-resolution intensity images. In the Fourier domain it is constrained by the pupil

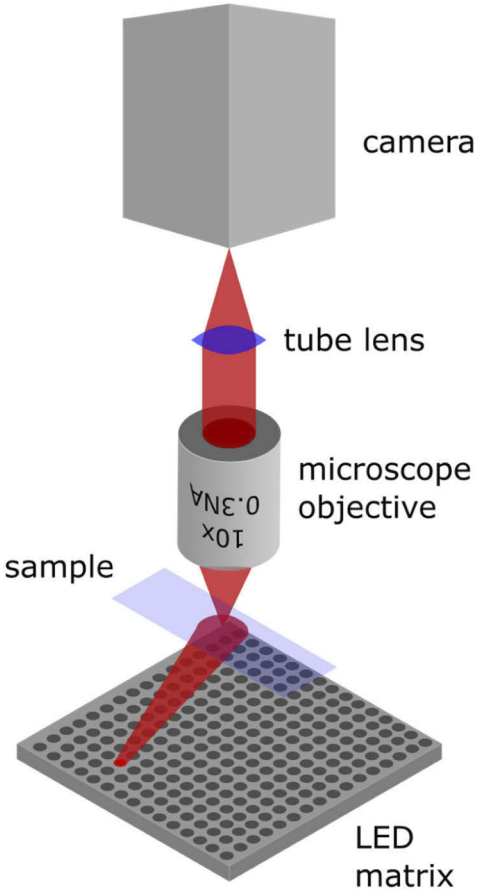

Fig. 1. Schematic of Fourier ptychography imaging. Scattering light from high angle LEDs allow high spatial frequencies in the sample to be imaged. By processing the images generated from all the individual LED illuminations (in a 15×15 array) a high-resolution quantitative phase image may be calculated.

Biomedical Optics EXPRESS

support function. Images collected at different incidence angles have pupil support functions that are shifted in position in the Fourier domain. The collection of low-intensity images collected at various incidence angles allows the pupil support function to scan the Fourier domain thereby generating a larger synthetic numerical aperture [26].

An addressable LED matrix with LEDs having spatial coherence over a sizable patch of the sample is used as an illumination source. Normally the resolution of an image is limited by the numerical aperture of the microscope objective. By illuminating with light emerging from outside the collection cone of the objective it is possible to image scattered light from the sample onto the detector (see Fig. 1). The scattering due to this high-angle illumination contains high spatial frequency contrast information of the sample. By systematically illuminating from low to high illumination angles an image with a synthetic numerical aperture that is greater than the optical numerical aperture of the objective can be generated. This high synthetic numerical aperture is what allows the Fourier ptychography to beat the resolution limit set by the optics. This is an advantage in diagnostic applications which can benefit from jointly having both a large-field of view and a high-resolution [27]. In our application of malaria parasite infected erythrocyte detection it allows a large number of cells to be imaged in one field of view while maintaining high-resolution detail for each cell. A low-cost 3D printed Fourier ptychography microscope using open-source hardware has also been demonstrated in the literature, making the technique potentially field deployable [28]. A recently published numerical scheme developed by Bianco *et al.* [29] has shown that Fourier ptychography can be performed on unaligned setups, thereby increasing the ease of use of the technique by untrained medical workers for point-of-care diagnostics applications.

2. Experimental method

2.1. Fourier ptychographic microscope

We built our Fourier ptychographic microscope on a Nikon TE-2 optical microscope. We used a 10x 0.3NA microscope objective for imaging. In addition an intermediate optic in the microscope allowing an additional 1.5x magnification was used. The trans-illuminator was replaced by a 32×32 LED matrix with a 4 mm pitch (Adafruit) and a central wavelength of 632 nm. The LED was centered at a height of 85 mm above the sample plane. The LED matrix was controlled by an Arduino microcontroller which was integrated with a LabView program that collected the image data in synchrony with the LED illumination durations. The central 15×15 LEDs were utilized for data collection (i.e. total of 225 images collected for each field of view). The exposure duration for each image in the image stack was 5s. It took approximately 20 minutes to collect an entire stack of images. The acquisition time could be significantly reduced by multiplexing the illumination [30]. The camera used was a cooled 16bit monochrome sCMOS unit with a 7.4 µm pixel size and 2560×2160 array dimensions (Andor, Zyla 5.5).

The LED positions used in the quantitative phase reconstruction algorithm were calibrated using an image analysis routine [31]. The image stack with calibrated LED positions was processed patch-wise to generate a high-resolution quantitative phase image [30] using an open source MATLAB program [32]. The patch size was 120×120 pixels and a 20 pixel overlap with adjacent patches was used. The constituent quantitative phase image patches were then stitched together using Fiji software to generate a final quantitative phase image of the whole field of view with dimensions of 7540×6340. We used a USAF test target to check the spatial resolution of our system (see Fig. 2). A cropped region of a low-resolution image from the image stack is shown in Fig. 2(A), while the reconstructed high-resolution Fourier ptychography phase image is shown in Fig. 2(B). The numerical aperture of the low-resolution image is 0.3. The spatial resolution of the low-resolution image is 2.1 µm. The synthetic numerical aperture for the reconstructed high-resolution image is 0.73 leading to a spatial resolution of 0.86 µm for our system. This resolution is too fine to confirm on our test grid.

Biomedical Optics EXPRESS

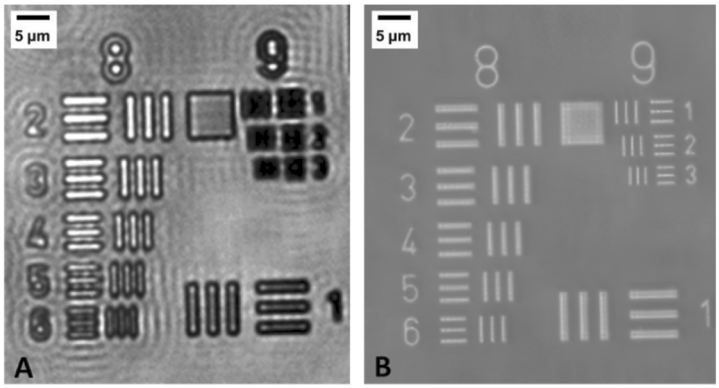

Fig. 2. Imaging of USAF spatial resolution test grid (group numbers 8 and 9) on our Fourier ptychography microscope. A. Low-resolution image. B. Reconstructed high-resolution Fourier ptychography phase image.

To check the quantitative phase imaging performance we imaged an SiO_2 phase calibration slide (PhaseFocus) with our Fourier ptychography microscope. The 303 nm high features were measured by quantitative phase imaging to have a feature height of 278 ± 44 nm (see Fig. 3). The standard deviation of the background phase value immediately surrounding the features was measured to be 0.165 rad (17 nm).

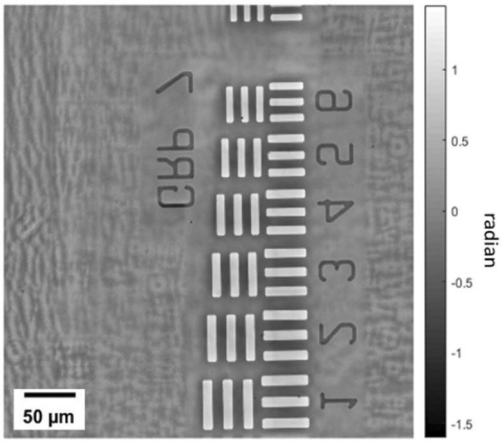

Fig. 3. Quantitative phase image of SiO_2 phase calibration slide with 303 nm tall relief features. The relief height measured from the optical pathlength difference was 278 ± 44 nm.

2.2. Sample preparation and measurement

We used Wistar rats (n=4) which we infected with *Plasmodium berghei* as our model system. Ethics board approval was obtained from Bezmialem Vakif University. Our *Plasmodium berghei* strain was genetically modified to express GFP (green fluorescent protein) in all life cycle stages, under the control of PbHSP70_1 constituitive promoter by deletion of the PbP230p dispensable gene in wild-type background (unpublished study). This wild-type like GFP expressing parasite clone was generated using the same method as described by Hart *et al.* [33]. The PbP230p(-) clones expressing GFP used in this study were stored as frozen stocks at −150C. Freshly thawed parasites were intra-peritoneally injected into the rats. We prepared thin-smear samples directly

Biomedical Optics EXPRESS

from blood collected from the rat's tail when parasitemia as determined by flow-cytometry reached at least 1% [34]. To measure the parasitemia on the flow cytometer 2 µl of blood was diluted by 1:200 in PBS (phosphate buffered saline) containing 2uL of 0.25IU/µl heparin and the percentage of erthothrocytes that emitted green fluorescence was determined. The thin-smear samples were coverslipped and placed on our Fourier ptychography microscope with fluorescence imaging capability. See Fig. 4 for a schematic of the microscope with fluorescence imaging and Fourier ptychography modalities. This figure shows the fluorescence imaging modality in effect with blue light emerging from the Hg arc lamp and reflected onto the sample by the dichroic mirror. This excites green fluorescence in the infected erythrocytes which is imaged onto the sCMOS detector. In Fourier ptychography imaging mode the LED matrix is used as the light source (632 nm) and the dichroic mirror is removed. Figure 5 shows an image of the microscope in our lab that was used for these experiments.

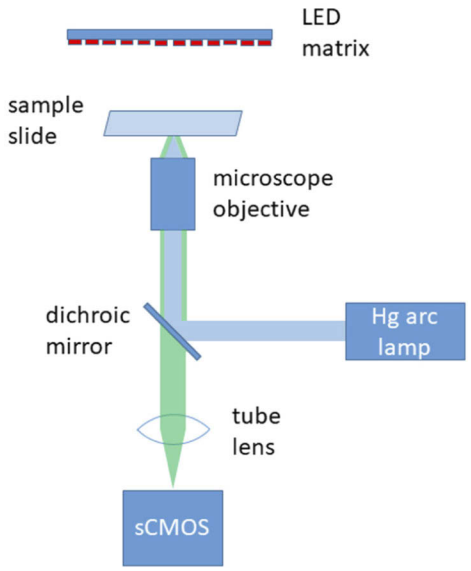

Fig. 4. This figure shows a schematic of our microscope with fluorescence and Fourier ptychography imaging modalities. Blue light emerging from the Hg arc lamp is reflected onto the sample by the dichroic mirror. This excites green fluorescence in the infected erythrocytes on the sample slide which is then imaged onto the sCMOS detector. The fluorescence images are used to locate the infected erythrocytes for determining the ground truth for training and testing models based on our Fourier ptychography method. In Fourier ptychography imaging mode the LED matrix is used as the light source (632 nm) and the dichroic mirror is removed.

We first took a fluorescence image of the blood sample allowing us to determine which cells are infected. The fluorescence image was thresholded to remove the background fluorescence. We then used the Fourier ptychography technique and recorded a stack of images collected at different illumination angles by successively turning on different LEDs in an LED matrix. This stack of images was then processed to generate a high-resolution quantitative phase image [30,31]. Cells were segmented in the quantitative phase image by using edge detection. The segmented cells were filtered by area to exclude the larger white blood cells present in the sample. The white blood cells similar in size to the erythrocytes were included in the analysis and constitute a small error in our method (<1% of the cells labeled as uninfected erythrocytes are actually white blood cells). The fluorescence image was then overlayed with the quantitative phase image (see Figs. 6 and 7). Cells in the quantitative phase image which overlapped with fluorescence signal in the

Biomedical Optics EXPRESS

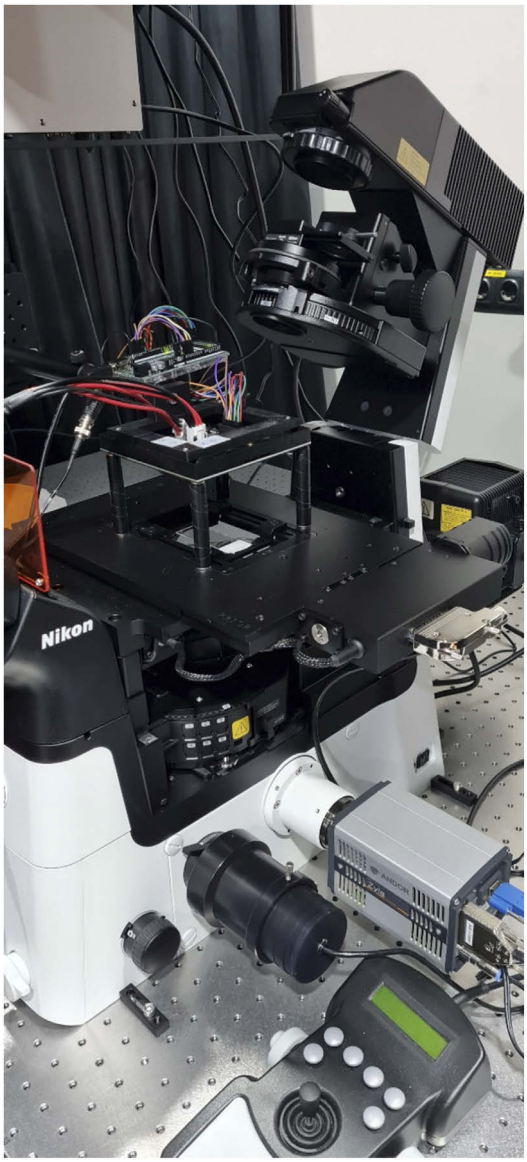

Fig. 5. Picture of our Fourier ptychography microscope with fluorescence imaging capability.

fluorescence image were labelled as infected, the rest of the cells were labelled as uninfected. The quantitative phase images of the infected and uninfected cells were then filtered by an area metric to remove cells with small segmented area as these were difficult to classify. We also removed cells that were mis-shapen or overlapping with each other based on their circularity metric. Overlapped cells accounted for approximately 1% of the total cell population. By applying a circularity threshold, these cells were removed (although not exclusively). In total about 10-12% of the cells were filtered out and not included in the subsequent machine learning and deep learning training and testing. We used the remaining labeled quantitative phase images of cells to train and test machine learning and deep learning models that we outline later. Image processing routines were written in MATLAB.

Biomedical Optics EXPRESS

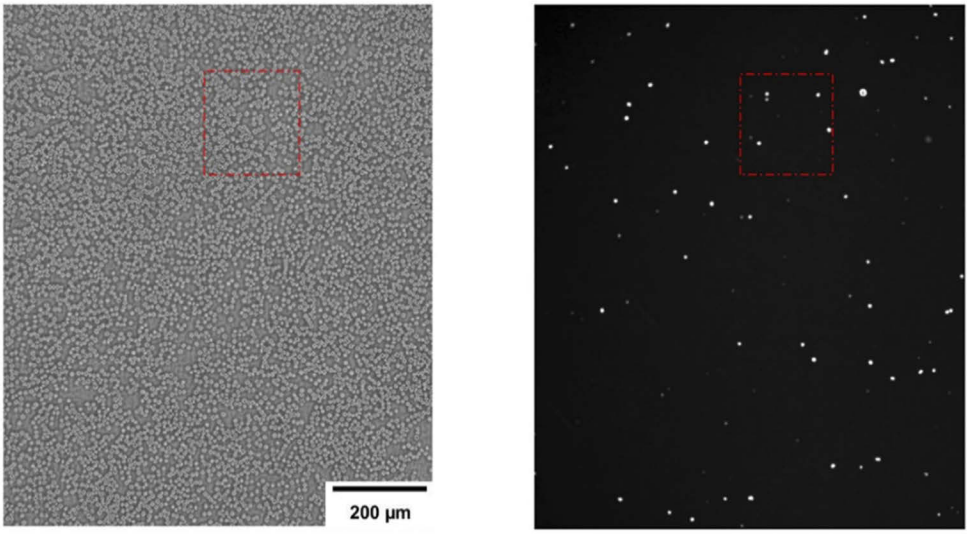

Fig. 6. Thin-smear blood sample imaged using fluorescence microscopy and then subsequently using Fourier ptychography. Overlay of quantitative phase and fluorescence images in the region indicated by dashed rectangle shown in Fig. 7.

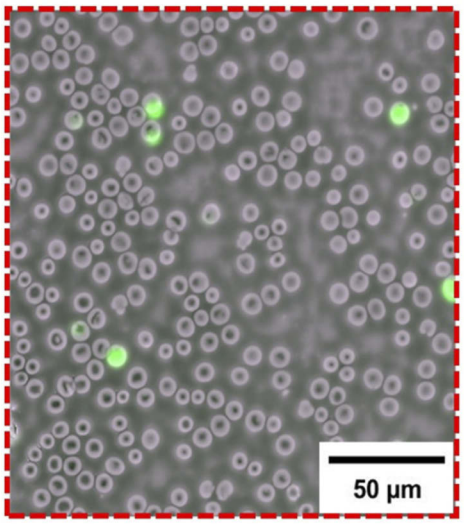

Fig. 7. A patch of the overlayed quantitative phase and fluorescence images taken from the field of view shown in Fig. 6 (see red dashed rectangle). Erythrocytes in the quantitative phase image which overlap with fluorescence (shown in green) are labelled as infected, the rest of the erythrocytes are labelled as uninfected. The labelled quantitative phase images of cells are then fed into machine learning and deep learning models to generate predictions based on only the quantitative phase image data.

2.3. Image processing

The cells in the full field of view quantitative phase image were segmented with the Canny method of edge detection. Each segmented cell was turned into a separate image for feature

Biomedical Optics EXPRESS

extraction and deep learning modeling. The individual cell image was 100×100 pixels large with the background padded with a gray level equivalent to the average background phase level measured for that field of view. This was calculated by creating a mask covering the background regions immediately adjacent to the cells. The average background phase level of this masked area was used for all the cells in the field of view. The overall phases of the 100×100 images of each segmented cell from all fields of view were each shifted so that all the background gray levels were identical. This operation preserved each cell's quantitative phase profile with respect to the background.

2.4. Machine learning method

We extract a combination of geometric/phase-morphologic and texture features from each of the labelled segmented cells to generate an 85 dimensional feature vector for each cell. A total of 22 geometric and phase-morphologic feature metrics are used for analysis here [19]. They include geometric features such as area and eccentricity as well as phase-morphologic features such as average phase, standard deviation of phase *etc.*. The remaining 63 features extracted from the quantitative phase image of the cells (100×100 pixels) are textural, 38 of these are LBP (local binary pattern) related features, 20 are GLCM (gray level co-occurence matrix) features and 5 are perceptual features. We used the MATLAB code referenced in [35] for calculating the textural features. We tried support vector machines, KNN and random forest models using Scikit-learn in Python and found that the random forest model performed the best. 3000 uninfected cells were selected at random and all 2325 infected cells that remained after filtering were utilized. Machine learning using the random forest model was repeated 4 times with test sets (20% of the cells) selected randomly each time with replacement between each sampling and the averaged results are reported.

2.5. Deep learning method

We tried ResNet50, DenseNet121 and VGG16 deep learning models and found that the VGG16 model performed the best. We trained the VGG16 deep learning model from scratch using 100×100 pixel quantitative phase images of each segmented cell. We used data augmentation to increase the infected cell image number used for training 10 fold from 1744 to 17440 by using rotations of 45°, 90°, 135° and 180° and flips about the vertical axis. 580 infected cell images were in the test set. A total of 21000 uninfected cell images were selected at random, 18000 were used for training and 3000 for testing. Four-fold cross validation was used to generate results. Averaged results are reported. Training was performed for 30 epochs during each trial using a learning rate of 0.00003. The cross-entropy loss metric was used along with the ADAM optimizer. Deep learning modeling was preformed using the Pytorch library on a GPU equipped PC. We also explored the effect of decreased resolution of the images on the deep learning results. We simulated decreased resolution by resizing the cell images 4x smaller and 10x smaller (in linear dimension), causing loss of higher resolution content. We then resized these cell images back up to the original 100×100 pixel sizes and performed the deep learning training and testing on the 4x and 10x reduced resolution images. In a separate analysis we also performed 4-fold cross validation based on stratification of each rat (4 rats were used in our experiments). In this case each fold was tested with images from a different rat (and trained with the remaining 3 rats' data).

3. Results

In total we examined 23 fields of view from infected blood samples from 4 rats. The parasitemia of these animals ranged from 2 to 11%. In each field of view we detected on average 6200 ± 2000 erythrocytes. Twenty randomly selected infected erythrocytes are shown in Fig. 8, and twenty randomly selected uninfected erythrocytes are shown in Fig. 9.

Biomedical Optics EXPRESS

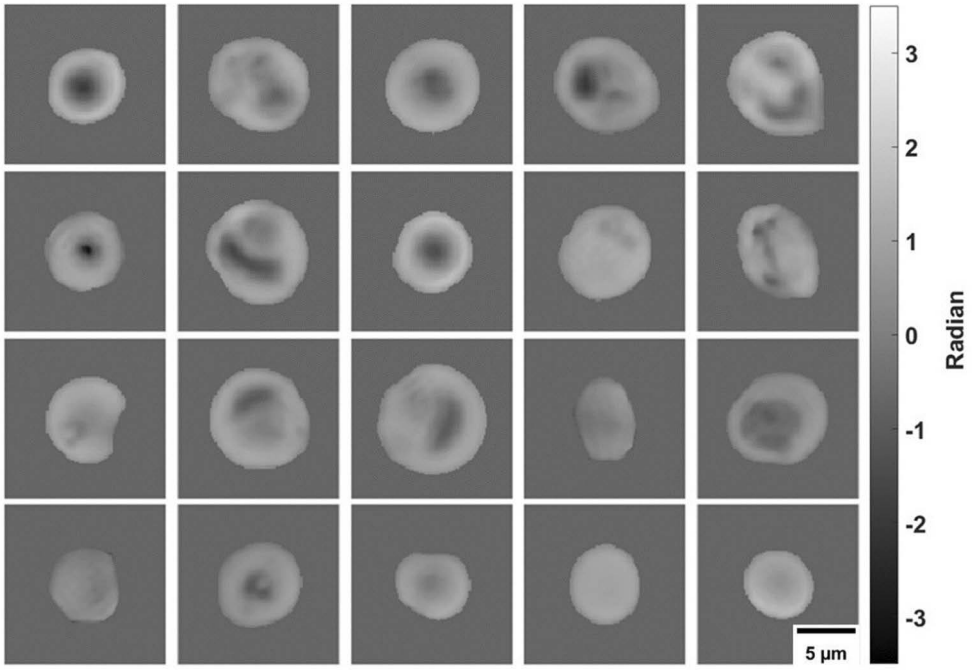

Fig. 8. Quantitative phase images of 20 randomly selected infected erythrocytes.

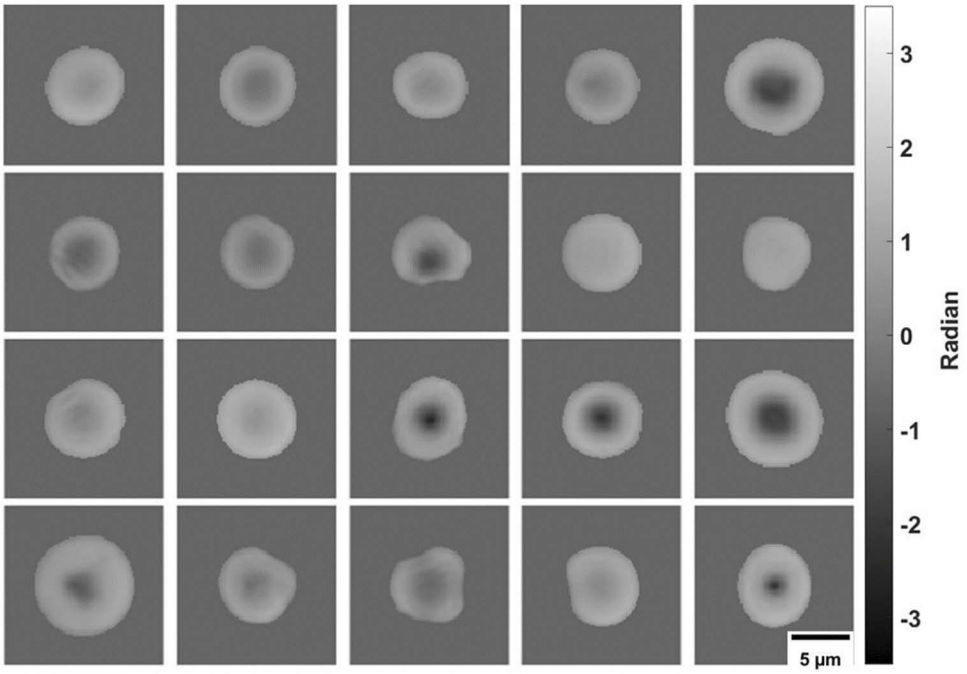

Fig. 9. Quantitative phase images of 20 randomly selected uninfected erythrocytes.

Biomedical Optics EXPRESS

Feature importance for the trained random forest model was determined using the impurity based method [36]. Figure 10 shows the importance of each of the 85 features along with the class the feature belonged to.

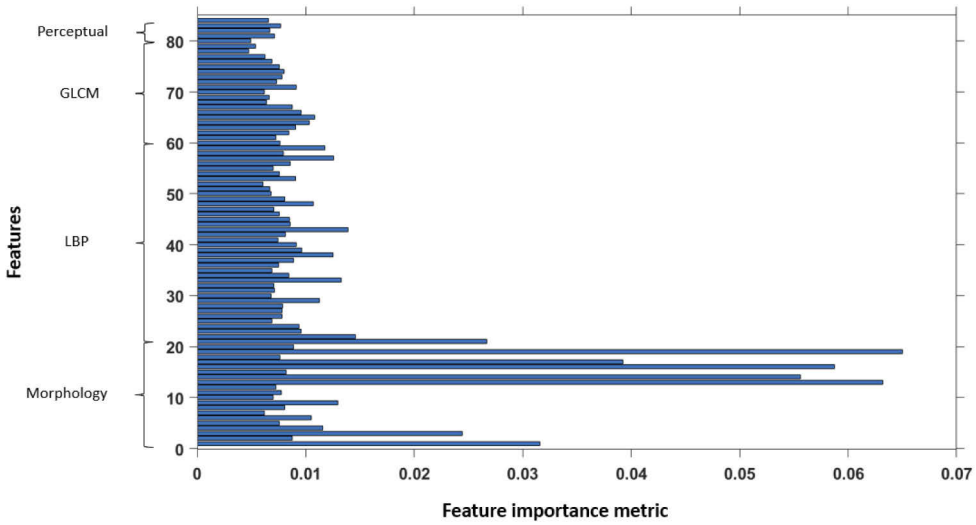

Fig. 10. Feature importance based on impurity-based method for all 85 features, organized according to feature group-type. The textural features used are represented by the LBP (local binary pattern), GLCM (gray-level co-occurrence matrix) and perceptual groups.

Histograms of infected and uninfected cells for eight of the top features are indicated in Fig. 11. Top non-redundant features were selected for display. For example while the area, perimeter and major axis length features are all highly ranked features according to feature importance using the impurity based method, their histograms look similar as they are all representing the underlying size distribution of the cells in slightly different ways. In this set only the area histogram is shown for demonstration purposes. Of these selected 8 top non-redundant features 5 are morphology based and 3 are texture based.

The area histogram shows a broader distribution in area values for the infected cells compared to the uninfected cells. In addition many infected cells have areas that are larger than the maximum uninfected cell area. The standard distribution histogram shows that the standard distribution of the phase values of the infected cells are biased to higher values than the uninfected cells' standard distribution. This is also expected from a visual inspection noting that the infected cells have a greater non-uniformity in their phase values. The average symmetry value is defined as in [19], where OPD refers to the optical pathlength difference (i.e. measured phase):

$$\text{average symmetry} = \frac{1}{2\pi}\int_0^{2\pi} \frac{OPD(x,y)\cdot OPD(x',y')}{||OPD(x,y)||^2} d\theta \tag{1}$$

$$\text{where} \begin{bmatrix} x' \\ y' \end{bmatrix} = \begin{bmatrix} \cos\theta & \sin\theta \\ -\sin\theta & \cos\theta \end{bmatrix} \begin{bmatrix} x \\ y \end{bmatrix}$$

Rotated replicas of the quantitative phase image of a rotationally asymmetric cell that is dissimilar to its unrotated counterpart results in lower average symmetry compared to rotationally symmetric cells. We see that the average symmetry feature of infected cells in Fig. 11 skews

Biomedical Optics EXPRESS

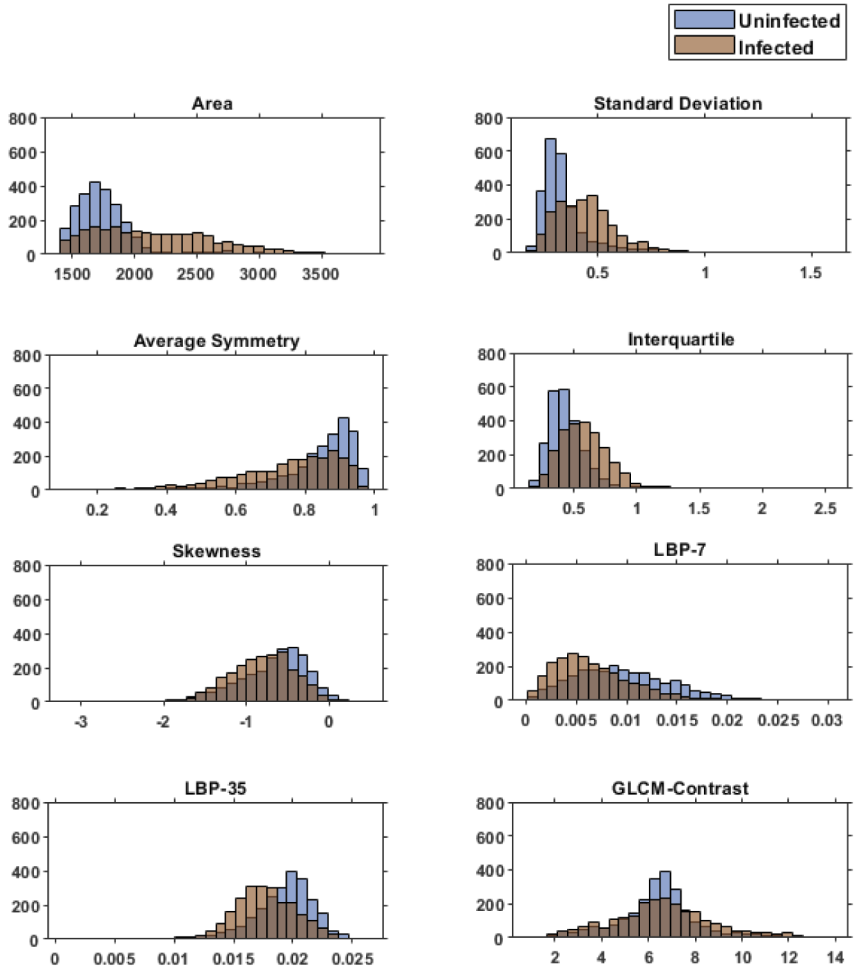

Fig. 11. Histograms of eight of the top non-redundant features. The morphology based features of area, standard deviation, average symmetry, interquartile and skewness are explained in [19]. The texture features LBP-7 and 35 are the 7th and 35th features in the local binary pattern features set used in the MATLAB code referenced in [35]. The texture feature GLCM-Contrast is the contrast related feature in the gray-level co-occurrence matrix feature set used in [35]. Histograms contain 2325 infected cells and 2325 uninfected cells.

to lower average symmetry values, indicating their decreased rotational symmetry compared to uninfected cells.

The interquartile feature looks at the average of the upper quartile of the quantitative phase distribution for each cell. The histogram of the interquartile feature for the uninfected and infected cells shows that the infected cells have, on average a slightly larger average phase value in the upper quartile, indicating that when comparing the thickest regions of the cells, the infected cells have slightly thicker cell structures.

The skewness indicates the amount of asymmetry in the histogram distribution. The histograms for this feature indicate that both uninfected and infected cell phase distributions are negatively skewed, with infected cells demonstrating slightly more negatively skewed distributions of their phase.

The texture features LBP-7 and 35 are the 7th and 35th features in the local binary pattern

Biomedical Optics EXPRESS

features set used in the MATLAB code referenced in [35]. These histograms indicate that these textural features are slightly higher in value for the uninfected cells. The texture feature GLCM-Contrast is the contrast related feature in the gray-level co-occurrence matrix feature set used in [35]. The histogram of this textural feature shows that the distribution is more sharply peaked for the uninfected cells, indicating a more narrow distribution of this feature compared to the infected cells.

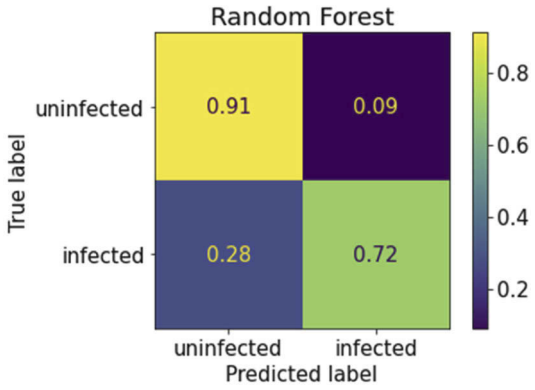

Fig. 12. Confusion matrix for random forest machine learning model test results (average of 4 trials). Data indicate fraction of cases. 458 cells were in the infected test group and 608 cells were in the uninfected test group for each trial.

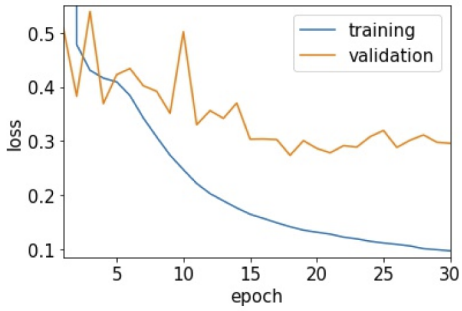

Fig. 13. Loss curve of training and validation data sets over 30 epochs for VGG16 deep learning model.

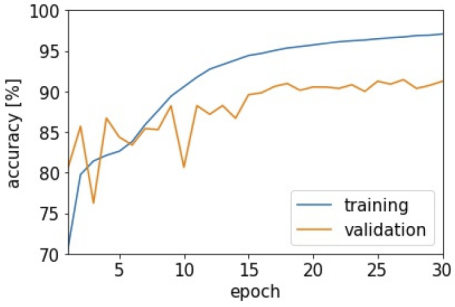

Fig. 14. Accuracy curve of training and validation data sets over 30 epochs for VGG16 deep learning model.

Biomedical Optics EXPRESS

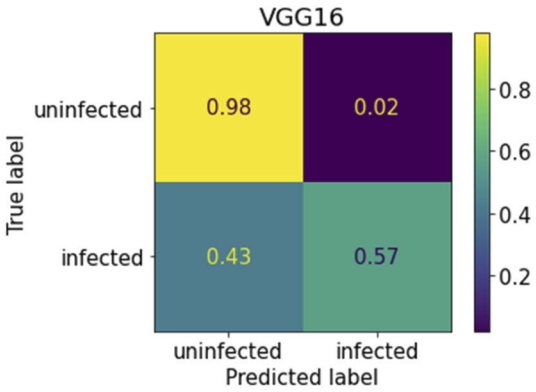

Fig. 15. Confusion matrix for VGG16 deep learning model results (average of 4 cross-validation trial results). Data indicate fraction of cases. 580 cells were in the infected test group and 3000 cells were in the uninfected test group for each trial.

The results of the trained random forest model test results using all 85 features are as follows: accuracy = 83%, F_1-score = 0.78, specificity = 91% and sensitivity = 72%. Figure 12 shows the confusion matrix.

The VGG16 deep learning loss and accuracy curves on the training and validation data sets over 30 epochs are shown in Figs. 13 and 14 respectively. The loss and accuracy curves for the VGG16 deep learning training indicate that the model has achieved a stable solution, with no improvement in performance past 20 epochs of training.

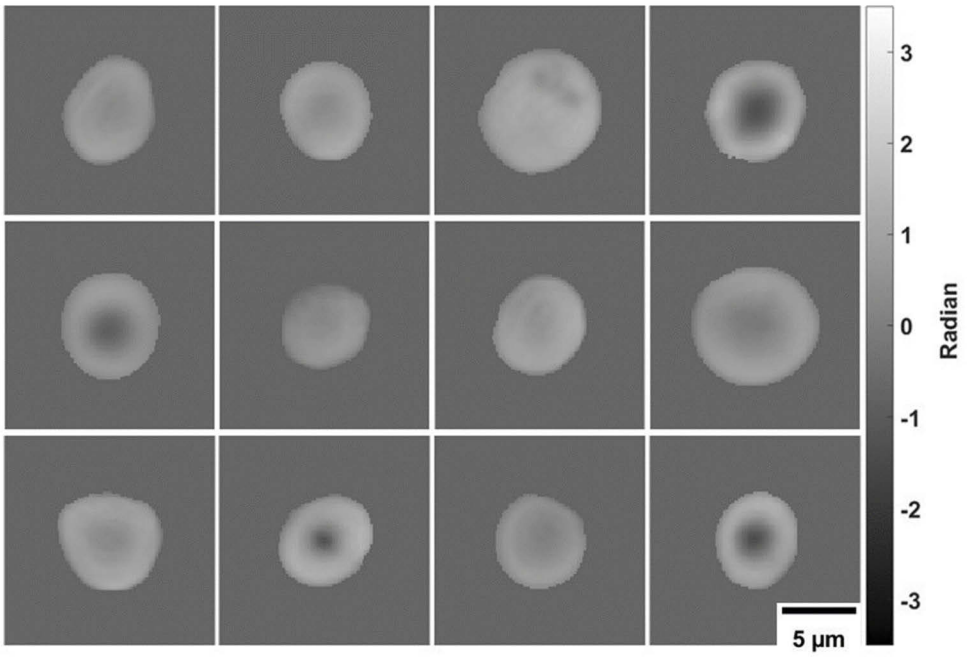

Fig. 16. Twelve randomly selected infected erythrocytes that were misclassified as uninfected by the VGG16 network.

Biomedical Optics EXPRESS

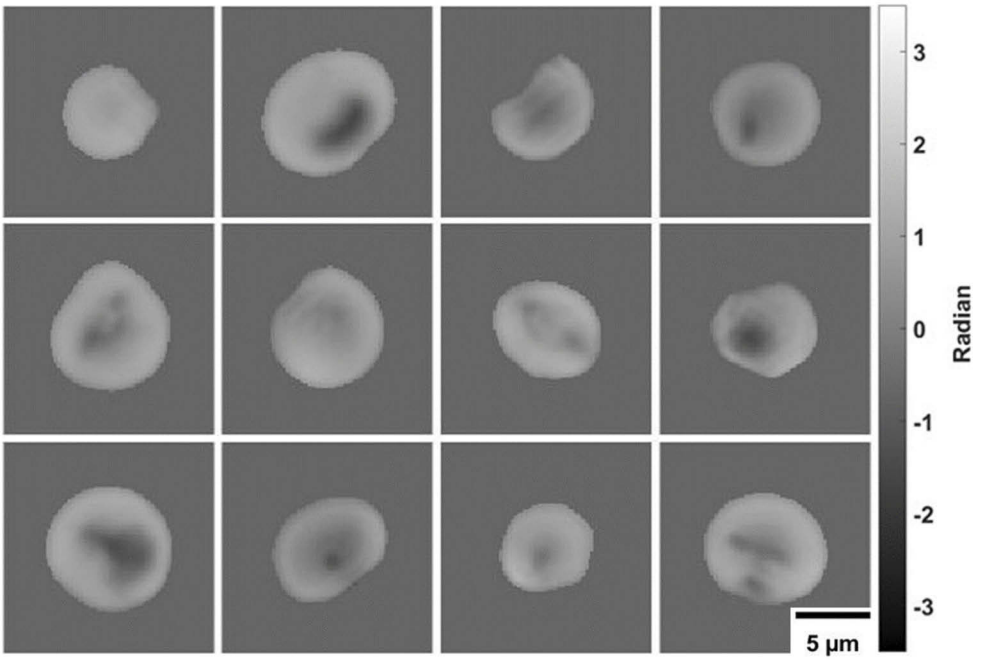

Fig. 17. Twelve randomly selected uninfected erythrocytes that were misclassified as infected by the VGG16 network.

The results of the trained VGG16 deep learning model test results (measured on the validation data set) are as follows: accuracy = 91%, F_1-score = 0.68, specificity = 98% and sensitivity = 57%. Figure 15 shows the confusion matrix. The results on the training data are as follows: accuracy = 97%, F_1-score = 0.97, specificity = 99% and sensitivity = 96%. We also retrained the VGG16 model for images at lower resolution, the model trained on images at 4x lower resolution yielded: accuracy = 90%, F_1-score = 0.67, specificity = 95%, sensitivity = 64%, while the model trained on images at 10x lower resolution yielded: accuracy = 88%, F_1-score = 0.62, specificity = 94%, sensitivity = 60%. The averaged results based on stratification by rat are as follows: accuracy = 81%, F_1-score = 0.46, specificity = 90% and sensitivity = 42%.

Twelve randomly selected infected erythrocytes that were misclassified as uninfected by our VGG16 network model are shown in Fig. 16. Twelve randomly selected uninfected erythrocytes that were misclassified as infected by our VGG16 network model are shown in Fig. 17.

4. Discussion

The feature strength of all 85 features used in our random forest model shown in Fig. 10 show that the set of morphology features, as a group, are the most useful. However we note that there are some textural features (in the LBP (local binary pattern) and GLCM (gray-level co-occurrence matrix) textural feature groups) that are better than some of the features in the morphology feature set, so they should not be overlooked. The histograms of eight of the top features shown in Fig. 11 indicate the distributions for the infected and uninfected cell populations. Other strong features that are not shown are perimeter, equivalent diameter, major-axis length, minor-axis length and minimum symmetry (see [19] for feature definitions).

The loss and accuracy curves (Figs. 13 and 14) for the VGG16 deep learning training indicate that the model has achieved a stable solution, with no improvement in performance past 20 epochs of training.

Biomedical Optics EXPRESS

The machine learning (random forest model) and the deep learning model (VGG16) yield specificities of 91% and 98% respectively. The sensitivities yielded are 72% for the random forest model and 57% for the VGG16 model. From Fig. 8 we can notice the large number of infected cells with asymmetric cell structures in their interior. These cells are significantly differentiated from the more symmetric looking cells structures of the uninfected group observed in Fig. 9. However, among the infected cells there are also a significant number of symmetric-like cells that are similar to their uninfected counterparts in Fig. 9. In Fig. 16 we can see how the VGG16 model's misclassified infected cells look like they are uninfected. These infected cells that look like they are still uninfected (from the quantitative phase image data) may be because they are in the early stages of infection where significant cell structure alterations that could be reflected in the quantitative phase image have not yet occurred. We believe that the poor sensitivities that both our machine learning and deep learning models yield are due to this phenomenon. We predict, from the fractions of infected cells misclassified in our models, that this non-discriminable early-stage fraction of infected cells is between 28-43% of the total infected erythrocyte population.

2% of the uninfected cells were misclassified by the VGG16 model as infected. A random sample of these misclassified cells are shown in Fig. 17. A good number of these cells look similar to their infected counterparts in Fig. 8. This type of misclassification is due to variabilities inherent in the sample preparation technique. During the smearing and drying process of the cells on the glass surface some small fraction of the cells are crumpled and misshapen and are mistakenly classified as infected. Decreasing this type of misclassification (i.e. increasing the specificity beyond 98%) could be addressed by having a larger training set.

The results of the deep learning low-resolution simulations indicate that lower-resolution only marginally decreases the performance of the deep learning model indicating that there is enough detail in even the reduced resolution images to classify cells similarly to the model based on the original images. The results based on stratification by rat show a more severe decrease in performance however. This indicates that there is significant heterogeneity in the rat to rat data which isn't well sampled in the training set by only 3 rats. A training set with a larger number of subjects would allow the model's training data to better sample the rat populations' heterogeneity and this should improve the performance of the subject stratified model.

Most mature malaria diagnostics techniques report their performance metrics in terms of subject-based sensitivities and specificities, *i.e.* how sensitively can a technique detect an infected individual in a population. The goals and experimental design of our study was aligned with ascertaining the cell-based sensitivities and specificities of the technique, a more basic question, *i.e.* how sensitively can our technique detect an infected cell in a population of cells. In the gold-standard technique of manual microscopic analysis of stained smears, it is assumed the identification of infected cells is performed with 100% sensitivity [37]. However, the clinical center to center discrepancies reported in the field [38] indicate that the actual cell-based performance of manual microscopy analysis many not be ideal as assumed. A label-free quantitative phase imaging based study that has reported cell-based sensitivities and specificities is that by Park *et al.* [19], though their numbers can't be directly compared to ours since they do not include cells in the early stage of infection in their measurement.

5. Conclusion

We have demonstrated an automated wide-field high-resolution method to detect malaria parasite infected erythrocytes in rats using a stain-free thin-smear preparation. We are able to image thousands of erythrocytes in a single field of view and make a determination of infection status of the quantitative phase image of each segmented cell based on machine learning (random forest) and deep learning (VGG16) models. In our random forest model we find that the morphology features out-perform textural ones, but note that some selected textural features are still useful.

Biomedical Optics EXPRESS

We also find that no model is clearly better, with the machine learning model having a higher sensitivity than the deep learning model, and the deep learning model having a higher specificity than the machine learning model. A hybrid approach could benefit from the strengths of both model types. Our reported sensitivities however are relatively low. This may be due to an inherent ambiguity in determining infection related quantitative phase image based feature changes in a significant fraction of the infected cell population as measured in thin-smears of whole blood samples. This non-discriminable fraction may be the subset of infected cells that are in the early stage of infection (e.g. ring-stage) where significant structural changes in the cell have not occurred yet. Making this fraction discriminable could require other sample preparation techniques or the addition of other imaging modalities.

Funding. National Institute of Allergy and Infectious Diseases (1R21AI111058-01A1); Türkiye Bilimsel ve Teknolojik Araştirma Kurumu (119Z409); Kalkinma Bakanliği (2015BSV036).

Disclosures. The authors declare that they do not have any conflicts of interest to disclose.

Data availability. Data underlying the results presented in this paper are not publicly available at this time but may be obtained from the authors upon reasonable request.

References

1. A. S. Aly, A. M. Vaughan, and S. H. Kappe, "Malaria parasite development in the mosquito and infection of the mammalian host," Annu. Rev. Microbiol. **63**(1), 195–221 (2009).
2. World Health Organization, "World malaria report 2020," (World Health Organization, 2020).
3. UNICEF, "Levels and trends in child mortality 2019," (2019).
4. C. Wongsrichanalai, M. J. Barcus, S. Muth, A. Sutamihardja, and W. H. Wernsdorfer, "A review of malaria diagnostic tools: mcroscopy and rapid diagnostic test (RDT)," Am. J. Trop. Med. Hyg. **77**(6_Suppl), 119–127 (2007).
5. P. Berzosa, A. de Lucio, M. Romay-Barja, Z. Herrador, V. Gonzalez, L. Garcia, A. Fernandez-Martinez, M. Santana-Morales, P. Ncogo, B. Valladares, M. Riloha, and A. Benito, "Comparison of three diagnostic methods (microscopy, RDT, and PCR) for the detection of malaria parasites in representative samples from Equatorial Guinea," Malar. J. **17**(1), 333 (2018).
6. J. A. Adegoke, A. De Paoli, I. O. Afara, K. Kochan, D. J. Creek, P. Heraud, and B. R. Wood, "Ultraviolet/visible and near-infrared dual spectroscopic method for detection and quantification of low-level malaria parasitemia in whole blood," Anal. Chem. **93**(39), 13302–13310 (2021).
7. F. Chen, B. R. Flaherty, C. E. Cohen, D. S. Peterson, and Y. Zhao, "Direct detection of malaria infected red blood cells by surface enhanced Raman spectroscopy," Nanomedicine **12**(6), 1445–1451 (2016).
8. M. Pukancsik, P. Molnar, A. Orban, A. Butykai, L. Marton, I. Kezsmarki, B. G. Vertessy, M. Kamil, A. Abraham, and A. S. I. Aly, "Highly sensitive and rapid characterization of the development of synchronized blood stage malaria parasites via magneto-optical hemozoin quantification," Biomolecules **9**(10), 579 (2019).
9. P. Lebel, R. Dial, V. N. P. Vemuri, V. Garcia, J. DeRisi, and R. Gomez-Sjoberg, "Label-free imaging and classification of live P. falciparum enables high performance parasitemia quantification without fixation or staining," PLoS Comput. Biol. **17**(8), e1009257 (2021).
10. T. Go, J. H. Kim, H. Byeon, and S. J. Lee, "Machine learning-based in-line holographic sensing of unstained malaria-infected red blood cells," J. Biophotonics **11**(9), e201800101 (2018).
11. Y. B. Zhang, H. C. Koydemir, M. M. Shimogawa, S. Yalcin, A. Guziak, T. R. Liu, I. Oguz, Y. J. Huang, B. J. Bai, Y. L. Luo, Y. Luo, Z. S. Wei, H. D. Wang, V. Bianco, B. H. Zhang, R. Nadkarni, K. Hill, and A. Ozcan, "Motility-based label-free detection of parasites in bodily fluids using holographic speckle analysis and deep learning," Light: Sci. Appl. **7**(1), 108 (2018).
12. G. Popescu, *Quantitative Phase Imaging of Cells and Tissues* (McGraw-Hill, 2011).
13. Y. Park, C. Depeursinge, and G. Popescu, "Quantitative phase imaging in biomedicine," Nat. Photonics **12**(10), 578–589 (2018).
14. G. Popescu, Y. Park, N. Lue, C. Best-Popescu, L. Deflores, R. R. Dasari, M. S. Feld, and K. Badizadegan, "Optical imaging of cell mass and growth dynamics," Am. J. Physiol. Cell Physiol. **295**(2), C538–C544 (2008).
15. Y. S. Kim, S. Lee, J. Jung, S. Shin, H. G. Choi, G. H. Cha, W. Park, S. Lee, and Y. Park, "Combining three-dimensional quantitative phase imaging and fluorescence microscopy for the study of cell pathophysiology," Yale J Biol Med **91**(3), 267–277 (2018).
16. I. Moon, A. Anand, M. Cruz, and B. Javidi, "Identification of malaria-infected red blood cells via digital shearing interferometry and statistical inference," IEEE Photonics J. **5**(5), 6900207 (2013).
17. A. Anand, V. K. Chhaniwal, N. R. Patel, and B. Javidi, "Automatic identification of malaria-infected rbc with digital holographic microscopy using correlation algorithms," IEEE Photonics J. **4**(5), 1456–1464 (2012).
18. A. Anand, I. Moon, and B. Javidi, "Automated disease identification with 3-D optical imaging: a medical diagnostic tool," Proc. IEEE **105**(5), 924–946 (2017).

Biomedical Optics EXPRESS

19. H. S. Park, M. Rinehart, K. A. Walzer, J. T. A. Chi, and A. Wax, "Automated detection of p. falciparum using machine learning algorithms with quantitative phase images of unstained cells," PLoS One **11**(9), e0163045 (2016).
20. M. Ugele, M. Weniger, M. Leidenberger, Y. W. Huang, M. Bassler, O. Friedrich, B. Kappes, O. Hayden, and L. Richter, "Label-free, high-throughput detection of P-falciparum infection in sphered erythrocytes with digital holographic microscopy," Lab Chip **18**(12), 1704–1712 (2018).
21. Y. Park, M. Diez-Silva, G. Popescu, G. Lykotrafitis, W. Choi, M. S. Feld, and S. Suresh, "Refractive index maps and membrane dynamics of human red blood cells parasitized by Plasmodium falciparum," Proc. Natl. Acad. Sci. U. S. A. **105**(37), 13730–13735 (2008).
22. B. Javidi, A. Markman, S. Rawat, T. O'Connor, A. Anand, and B. Andemariam, "Sickle cell disease diagnosis based on spatio-temporal cell dynamics analysis using 3D printed shearing digital holographic microscopy," Opt. Express **26**(10), 13614–13627 (2018).
23. T. O'Connor, A. Anand, B. Andemariam, and B. Javidi, "Deep learning-based cell identification and disease diagnosis using spatio-temporal cellular dynamics in compact digital holographic microscopy," Biomed. Opt. Express **11**(8), 4491–4508 (2020).
24. G. A. Zheng, R. Horstmeyer, and C. H. Yang, "Wide-field, high-resolution Fourier ptychographic microscopy," Nat. Photonics **7**(9), 739–745 (2013).
25. P. C. Konda, L. Loetgering, K. C. Zhou, S. Q. Xu, A. R. Harvey, and R. Horstmeyer, "Fourier ptychography: current applications and future promises," Opt. Express **28**(7), 9603–9630 (2020).
26. G. A. Zheng, C. Shen, S. W. Jiang, P. M. Song, and C. H. E. Yang, "Concept, implementations and applications of Fourier ptychography," Nat. Rev. Phys. **3**(3), 207–223 (2021).
27. R. Horstmeyer, X. Z. Ou, G. A. Zheng, P. Willems, and C. H. Yang, "Digital pathology with Fourier ptychography," Comput. Med. Imag. Grap. **42**, 38–43 (2015).
28. T. Aidukas, R. Eckert, A. R. Harvey, L. Waller, and P. C. Konda, "Low-cost, sub-micron resolution, wide-field computational microscopy using opensource hardware," Sci. Rep. **9**(1), 1 (2019).
29. V. Bianco, B. Mandracchia, J. Bhal, D. Barone, P. Memmolo, and P. Ferraro, "Miscalibration-tolerant Fourier ptychography," IEEE J. Sel. Top Quant. **27**(4), 1–17 (2021).
30. L. Tian, X. Li, K. Ramchandran, and L. Waller, "Multiplexed coded illumination for Fourier ptychography with an LED array microscope," Biomed. Opt. Express **5**(7), 2376–2389 (2014).
31. R. Eckert, Z. F. Phillips, and L. Waller, "Efficient illumination angle self-calibration n Fourier ptychography," Appl. Opt. **57**(19), 5434–5442 (2018).
32. https://github.com/Waller-Lab/FPM.
33. R. J. Hart, L. Lawres, E. Fritzen, C. Ben Mamoun, and A. S. I. Aly, "Plasmodium yoelii vitamin B-5 pantothenate transporter candidate is essential for parasite transmission to the mosquito," Sci. Rep. **4**(1), 5665 (2015).
34. A. S. I. Aly, G. Deveci, I. Yilmaz, A. Abraham, A. Golshan, and R. J. Hart, "Phenotypic analysis of rodent malaria parasite asexual and sexual blood stages and mosquito stages," Jove-J Vis Exp (2019).
35. J. N. Kather, C. A. Weis, F. Bianconi, S. M. Melchers, L. R. Schad, T. Gaiser, A. Marx, and F. G. Zollner, "Multi-class texture analysis in colorectal cancer histology," Sci. Rep. **6**(1), 27988 (2016).
36. E. Scornet, "Trees, forests, and impurity-based variable importance," arXiv preprint arXiv:2001.04295 (2020).
37. F. B. Tek, A. G. Dempster, and I. Kale, "Computer vision for microscopy diagnosis of malaria," Malar. J. **8**(1), 153 (2009).
38. B. Ngasala and S. Bushukatale, "Evaluation of malaria microscopy diagnostic performance at private health facilities in Tanzania," Malar. J. **18**(1), 375 (2019).